ATLAS NOTE

July 28, 2010

Tracking Studies for b-tagging with 7 TeV Collision Data with the ATLAS Detector

The ATLAS Collaboration

Abstract

The ability to identify jets containing b-hadrons is important for the physics program of ATLAS. This capability relies on the precise measurements of the parameters of charged tracks provided by the ATLAS Inner Detector. Using the 7 TeV collision data collected by the experiment in early 2010 and improved alignment and a more precise error description with respect to previous data taking periods, the tracking performance of the ATLAS Inner Detector has been assessed. Some of the studies relevant for b-tagging are discussed in this note, in particular the track properties and notably the impact parameter resolution.

1 Introduction

Identifying jets stemming from the hadronization of b-quarks is important for the physics program of a general-purpose experiment at the LHC such as ATLAS [1]. It is in particular useful to select very pure top quark samples, to search for new physics (supersymmetry, heavy gauge bosons, etc.), to search for and study Standard Model or SUSY Higgs bosons, and to veto the large $t\bar{t}$ background for many physics channels.

The LHC started to deliver collisions at 7 TeV centre-of-mass energy at the end of March 2010, and the ATLAS experiment is expected to collect a sizeable amount of data at this energy within the coming months. A major goal of early physics analyses is the measurement of top quark production in a currently unexplored center-of-mass energy range. However, the lower the centre-of-mass energy, the less favourable the signal over background ratio becomes for the measurement of the $t\bar{t}$ production cross-section. Requiring one jet to be b-tagged significantly reduces the background from W+ light jets at a modest cost to signal efficiency, typically improving the S/B ratio by at least a factor of 2. It is thus particularly useful to commission the b-tagging as early as possible.

b-jets can be identified either inclusively by measuring the impact parameters of the tracks (*i.e.* the distance of closest approach of the track to the collision point) from the b-hadron decay products, or explicitly by reconstructing the displaced vertex. In both cases, the precise measurement of the parameters of charged tracks in the ATLAS Inner Detector is a key ingredient.

An assessment of the performance of the tracking with the 7 TeV collision data is discussed in this note. The implications for lifetime-based tagging algorithms are discussed in Refs. [2]-[3]. Results obtained with 900 GeV collision data were reported in Ref. [4] and with earlier 7 TeV collisions in Ref. [5]. Improvements since [5] are the use of a more precise error description and refined alignment in the silicon detectors and higher integrated luminosity.

2 Data sample and event selection

The analyses are based on a sample of proton-proton collisions at $\sqrt{s} = 7$ TeV collected between March and June 2010. The sample corresponds to an integrated luminosity of about 15 nb^{-1} of data. The trigger used to select events for this analysis is the jet trigger with the lowest E_T threshold at the first trigger level [6]. This trigger currently requires at least one jet candidate object with $E_T > 5$ GeV at the electromagnetic scale, where no hadronic jet energy correction is applied, and is referred to as J5. At the analysis level at least one jet with $E_T > 20$ GeV is required. The jet energy is calibrated according to the offline electromagnetic calibration of the ATLAS calorimeters, but, in addition, a p_T and η dependent calibration factor is applied, to obtain the corrected hadronic jet energy scale [7].

Experimental data are compared to dijet Monte Carlo simulation, based on the PYTHIA event generator [8]. Experimental and simulated data were reconstructed according to the version of the ATLAS reconstruction software frozen in May 2010, using improved alignment constants and a more precise cluster error description in the Inner Detector. In particular, the cluster errors used for the early commissioning of the Inner Detector at $\sqrt{s} = 900$ GeV were based on very *broad* errors, reflecting a uniform distribution corresponding to the size of the cluster considered, while the new error description makes use of a more complete parameterization of the errors as a function of the track azimuthal incidence angle and of the cluster size. The simulated geometry corresponds to a perfectly aligned detector.

Only data collected during stable beam periods in which the silicon systems were operated at full depletion voltage are used. As part of the trigger selection, the Beam Pick-up probes are required to fire in correspondence of Bunch Crossing Identifiers compatible with collision events, thus removing spurious beam-halo events.

Events are required to have a reconstructed primary vertex with at least 10 tracks, while events with

one or more additional reconstructed primary vertices with more than 4 tracks are removed from the sample to reduce the influence of pile-up, as described more in detail in the next section. Additional low-p_T tracks provided by a dedicated pattern-recognition algorithm were also used for the primary vertex reconstruction. A data sample of 2.5 million events was obtained.

3 Primary vertex reconstruction

The average number of proton-proton interactions per bunch crossing, μ, ranges from ≈ 0.001 to ≈ 0.5, giving rise to pile-up, i.e. to at least two interactions per bunch crossing, in a fraction $\approx \frac{\mu}{2}$ of the events of the data sample used in this study[1]. The primary vertex reconstruction is designed to deal with pile-up by reconstructing multiple vertices.

Only tracks fulfilling the following basic track quality selection are used as an input to the primary vertex reconstruction algorithm:

- $p_T > 150$ MeV

- $|d_0| < 4$ mm (transverse impact parameter computed with respect to the beam spot center)

- $\sigma(d_0) < 5$ mm (error on the transverse impact parameters)

- $\sigma(z_0) < 10$ mm (error on the longitudinal impact parameters)

- ≥ 4 hits in the SCT (silicon micro-strip) detector

- ≥ 6 hits in the pixel and SCT detectors

An *iterative* vertex finding algorithm is used: after the track selection is applied, a new vertex seed is found by looking for the global maximum in the distribution of the z coordinates of the tracks at the point of closest approach to the beam spot center in the transverse plane. The new vertex position is then determined by passing the seed position and the tracks around the seed to the vertex fitting algorithm. Afterwards, only tracks incompatible with any previously found vertices by more than $\approx 7\sigma$ (corresponding to a cut on $\chi^2 > 49$) are used to seed a new vertex and this procedure is repeated until no tracks are left in the event and no additional vertices can therefore be found. The vertex fitting algorithm relies on the *adaptive* vertex fitter [9], which is a robust χ^2 based fitting algorithm which deals with outlying track measurements by down-weighting their contribution to the overall vertex χ^2 progressively, while the fit iterations proceed according to a fixed number of steps (fixed annealing scheme).

The beam spot center and size is used both during the finding step and as a constraint in the vertex fit. The beam spot width in the 7 TeV runs varies between ≈ 60 μm for the first runs ($\beta^* = 10$ m) and ≈ 30 μm for the runs with squeezed beams ($\beta^* = 2$-5 m), with a small increase in the width during the fills due to the growth in emittance of the beams. The bunch length results into a luminous region length of $\approx 20 - 50$ mm, depending on machine parameters, with very small variations within a run.

In the vertex fit, the beam spot constraint has a significant impact on vertices reconstructed starting from very few tracks, where the transverse resolution is dominated by the beam spot information. However, in the z direction, the length of the luminous region has no visible effect on the longitudinal resolution of the primary vertices, which is determined by the intrinsic longitudinal track resolution of the tracks feeding the primary vertices reconstruction.

To reduce the effect of multiple interactions during one bunch crossing no other primary vertices with more than 4 tracks are allowed in the same event. This is important for b-tagging purposes, since in the case of multiple interactions it may happen that the wrong vertex is selected as the main event

---

[1]assuming a Poisson distribution of the number of collisions per bunch crossing.
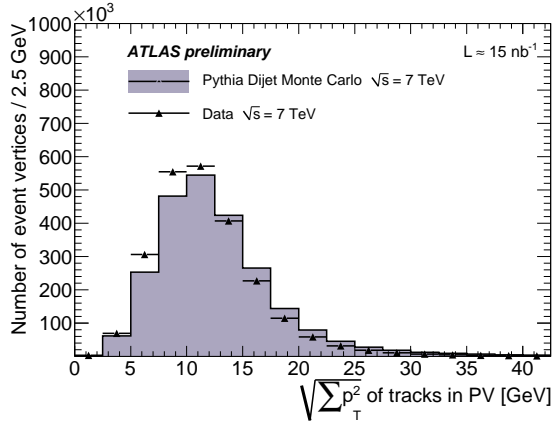
(a) Distribution of the $\sqrt{\sum p_T^2}$ from all tracks in the event vertex.
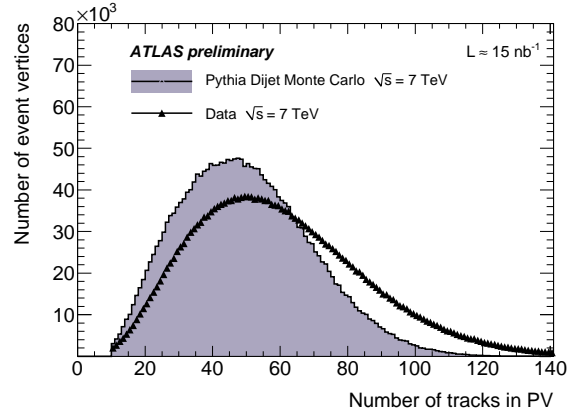
(b) Number of tracks associated with the event vertex.

Figure 1: Basic properties of reconstructed primary vertices PV. Experimental data (solid black dots) are compared to the Monte Carlo simulation (plain histograms). Simulated data have been normalized to the experimental data.

vertex: this affects both the impact parameters of the tracks, which are computed with respect to the primary vertex, and the search for secondary vertices. The main event vertex is identified by choosing the primary vertex with the highest $\sum_{i=1}^{n_{\text{tracks}}} p_{T,i}^2$. The square root of this distribution $\sqrt{\sum p_T^2}$ for the main event vertex is presented in Fig. 1(a). Simulated data in Figs. 1(a) and 1(b) have been normalized to the experimental data.

The cut at four tracks was chosen to avoid a substantial number of incorrectly reconstructed primary vertices being interpreted as real additional pile-up interactions: these low track multiplicity vertices originate typically either from tracks which fail to be associated to the main event vertices or due to secondary vertices which are reconstructed within the beam spot size. In addition, to minimize the impact of the longitudinal vertex resolution on the impact parameter studies, the main event vertex is required to have at least 10 tracks. The number of tracks associated to the primary vertex is shown in Fig. 1(b). A significant disagreement is visible between experimental and simulated data. This disagreement points to the incorrect description of the number of primary and secondary particles in the simulation, especially at low p_T. This has also been shown in [10].

4 Track properties

The tracks reconstructed in the ATLAS Inner Detector [11] are the main ingredient for *b*-tagging. On average a track consists of 3 pixel hits, 4 space-points (*i.e.* 8 hits) in the silicon micro-strip detector and about 34 hits in the Transition Radiation Tracker (TRT). The innermost pixel layer (called also layer-0 or the *b*-layer) is located at a radius of 5 cm, while the TRT extends up to a radius of 1 m. The tracker is immersed in a 2 T magnetic field generated by the central solenoid. The intrinsic measurement accuracy of the pixels is around 10 μm in $r\phi$ and 115 μm in z. The tracker can measure the tracks efficiently and with good accuracy within $|\eta| < 2.5$ and down to $p_T \sim 150$ MeV.

Several pattern-recognition strategies are used to reconstruct tracks in the Inner Detector. In the following, the tracks from the "inside-out" approach [12] are used: the pattern-recognition starts in the two silicon systems and tracks are extended to higher radii. They are not required to have hits in the TRT. This algorithm reconstructs tracks with $p_T \geq 150$ MeV.

4.1 Baseline track selection

The track selection for *b*-tagging as already discussed in [1] is designed to select well-measured tracks and reject fake tracks and tracks from long-lived particles (K_S^0, Λ or other hyperon decays) and material interactions (photon conversions or hadronic interactions).

At least seven precision hits (pixel or micro-strip hits) are required. In addition, at least two hits in the pixel detector are required of which one must be in the innermost layer. A successful extension of the track into the TRT detector is not explicitly required, but is fulfilled by most tracks within its acceptance. The transverse and longitudinal impact parameters computed with respect to the primary vertex must fulfil $|d_0| < 1$ mm and $|z_0 \sin\theta| < 1.5$ mm respectively, θ being the track polar angle. Only tracks with $p_T > 1$ GeV are considered.
The total number of tracks after these cuts is about 23 million. This selection is used by the impact parameter tagging algorithms while slightly different selections are used by the secondary vertex algorithms as described in [3]. All the following results are using this selection, unless mentioned otherwise when it was mandatory to relax some of the criteria to study a particular effect.

4.2 Overall hit patterns

The patterns of hits on tracks have been studied using the experimental data and compared to Monte Carlo simulated data. The distribution of the total number of pixel hits on a track is shown in Fig. 2(a), and the distribution of the number of hits in the first pixel layer is shown in Fig. 2(b). The hit in the first pixel layer determines the resolution of the impact parameter of the track and is therefore essential for *b*-tagging. Figure 2(c) shows the distribution of the number of hits in the SCT detector on a track. The simulated data in all three hit distributions have been normalized to data and describes the experimental data very well. The discrepancies for the number of SCT hits on the track are being investigated.

The distribution of the average number of hits in the pixel system and in the SCT detector as a function of the track azimuthal angle and pseudorapidity are shown on Fig. 3. The simulated events describe well the experimental data. There are slight discrepancies between data and Monte Carlo for the number of pixel hits on track: only one configuration of dead pixel modules was simulated while the number of dead modules fluctuated over the period of data considered, and this distribution is sensitive to this effect.

The number of TRT hits on a track is not shown in this note, but agree well between experimental and simulated data.

4.3 The innermost pixel layer

The *b*-tagging quality cuts for tracks require a hit on the innermost pixel layer, which, thanks to its small radius, provides a precise measurement of the track impact parameter. It is therefore important to study how often a hit in this layer is attached to a track. To do so, the requirement of a hit on the innermost pixel layer is removed, but all other *b*-tagging quality cuts are retained. The fraction of *b*-tagging tracks which have such a hit is shown as a function of the track azimuthal angle and pseudo-rapidity in Figs. 4(a) and 4(b), respectively. Tracks crossing non-instrumented regions in the innermost pixel layer or regions with a dead module or dead front-end were discarded.

The plots show that the overall fraction of tracks which could have had an innermost pixel layer hit but do not have one is of the order of 0.5 %. Simulation and data agree reasonably well, though the fraction of tracks with an attached innermost pixel layer hit is slightly higher for the experimental data around $\eta = 0$. This is most probably due to a slightly too high fraction of pixels randomly killed in the simulation: further studies are on-going.
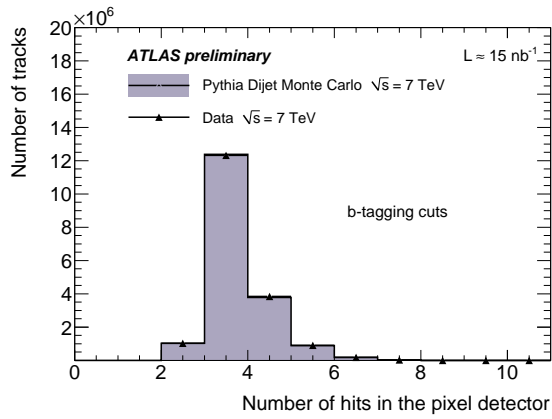
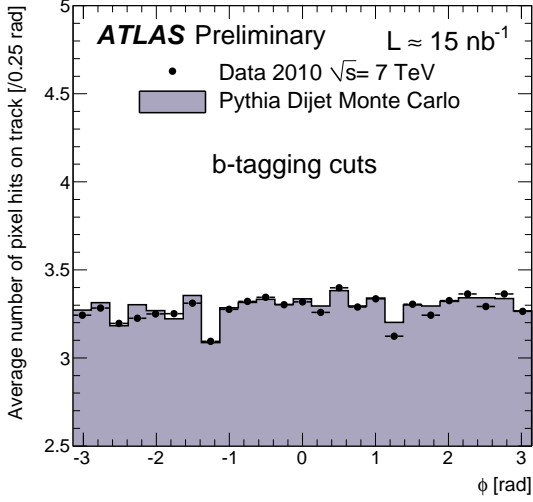(a) Number of pixel hits on a track.
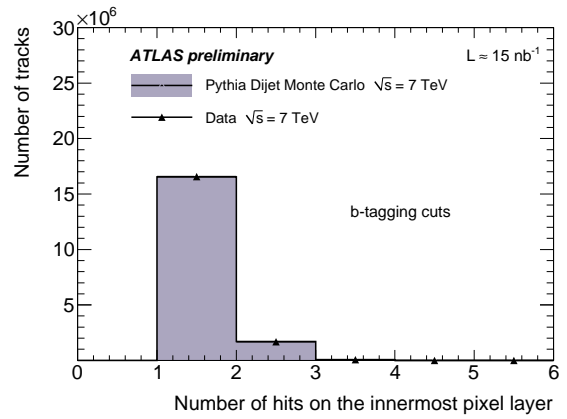
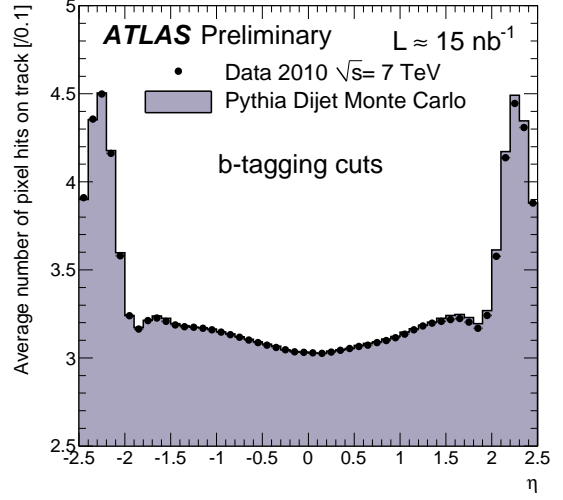(b) Number of pixel hits on a track in the first pixel layer.
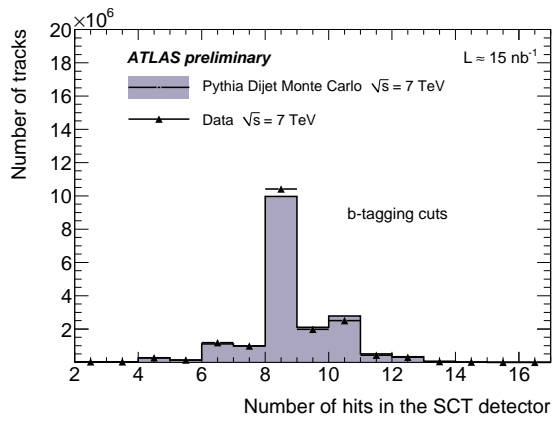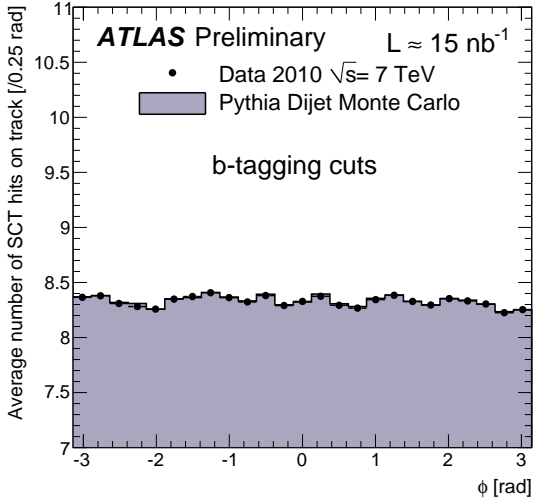

(c) Number of SCT hits on a track.

Figure 2: Distribution of number of pixel and SCT hits on tracks, for tracks fulfilling the *b*-tagging quality cuts. Experimental data (solid black dots) is compared to the Monte Carlo simulation (plain histogram). Simulated data have been normalized to the experimental data.
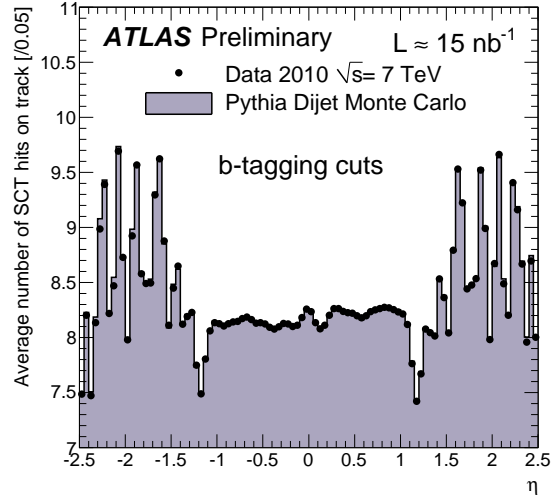
(a) Number of pixel hits versus track azimuthal angle.

(b) Number of pixel hits versus track pseudorapidity.

(c) Number of SCT hits versus track azimuthal angle.

(d) Number of SCT hits versus track pseudorapidity.

Figure 3: Distribution of the number of pixel and SCT hits as a function of the track azimuthal angle and pseudorapidity, for tracks fulfilling the *b*-tagging quality cuts. Experimental data (solid black dots) is compared to the Monte Carlo simulation (plain histogram).

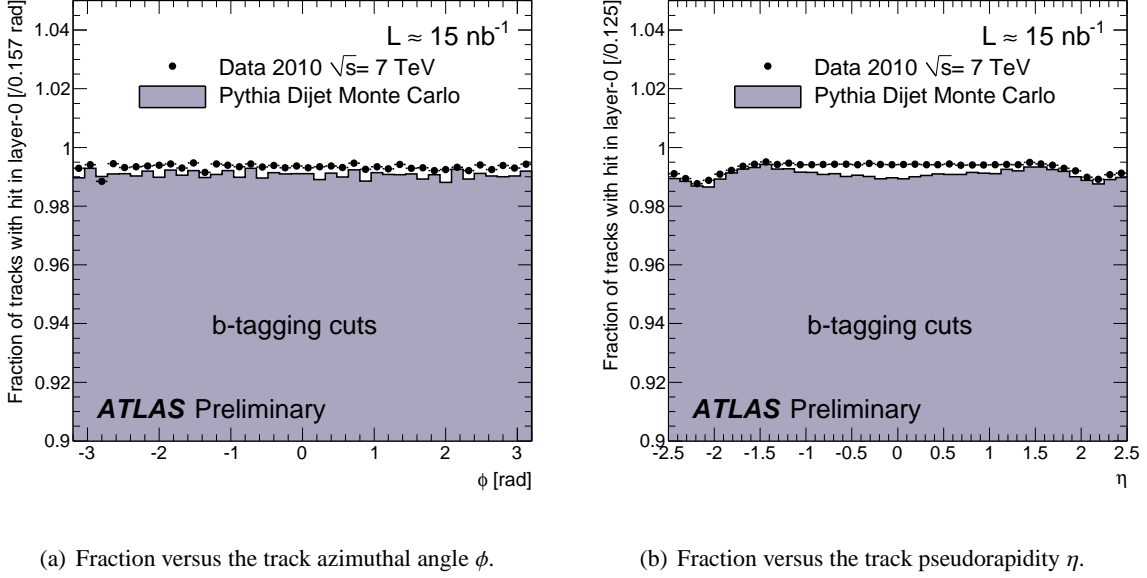(a) Fraction versus the track azimuthal angle ϕ.   (b) Fraction versus the track pseudorapidity η.

Figure 4: Distribution of the fraction of tracks having at least one hit on the first pixel layer, while fulfilling all the other b-tagging quality criteria, as a function of the track azimuthal angle ϕ and pseudorapidity η, for tracks crossing an active region. Experimental data (solid black dots) are compared to the Monte Carlo simulation (plain histogram).

4.4 Basic impact parameter distributions

The transverse impact parameter of a track, d_0, *i.e.* its distance of closest approach on the transverse plane to the primary vertex, is a key-ingredient for discriminating tracks originating from displaced vertices from tracks originating from the primary vertex. The longitudinal location z_0 at the same point of closest approach is also useful for the same reasons.

The distribution of d_0 for tracks fulfilling the b-tagging quality cuts is shown in Fig. 5(a), and its significance d_0/σ_{d_0} in Fig. 5(b). The distance d_0 is measured with respect to the primary vertex in an unbiased way: if the track under consideration was used for the primary vertex determination, it is first removed from the primary vertex which is subsequently refitted, and d_0 is computed with respect to this new vertex. The overall agreement between data and simulation is good, though the simulated distribution of d_0 is a bit narrower. It should be also noted that relating the d_0 distribution shown in Fig. 5(a) (and on subsequent figures as well) to the purely track-based d_0^{track} resolution is not straightforward since it is convolved with the resolution on the primary vertex position: $\sigma^2(d_0) = \sigma^2(d_0^{\text{track}}) + \sigma^2(d_0, \text{PV})$, where $\sigma(d_0, \text{PV})$ is the projection of the primary vertex error along the axis of closest approach of the track to the primary vertex on the transverse plane. This is further discussed in Section 5.

The distribution of z_0 for tracks fulfilling the b-tagging quality cuts is shown in Fig. 5(c), and its significance z_0/σ_{z_0} in Fig. 5(d). The measurement is again done in a unbiased way and the agreement between data and simulation is very good. Again the purely track-based resolution is here convolved with the resolution on the longitudinal position of the primary vertex.
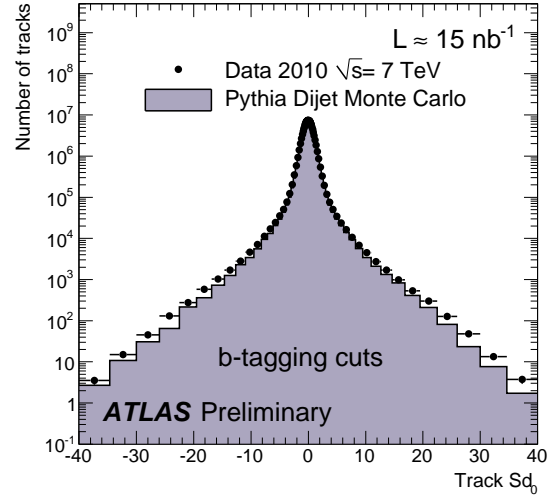
5 Impact parameter resolution

The knowledge of the impact parameter resolution is crucial for the correct understanding of the b-tagging algorithms and their performance. It has therefore been studied in great detail.
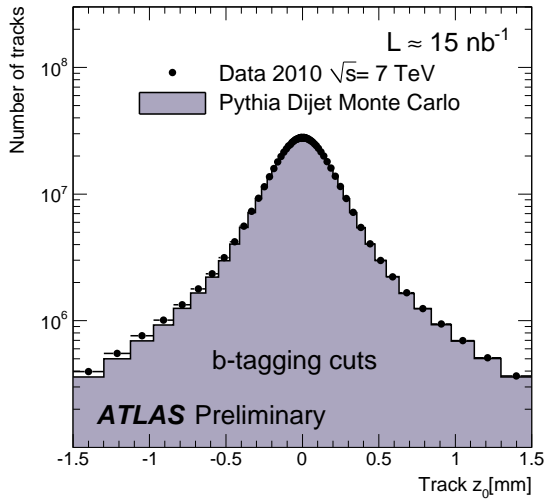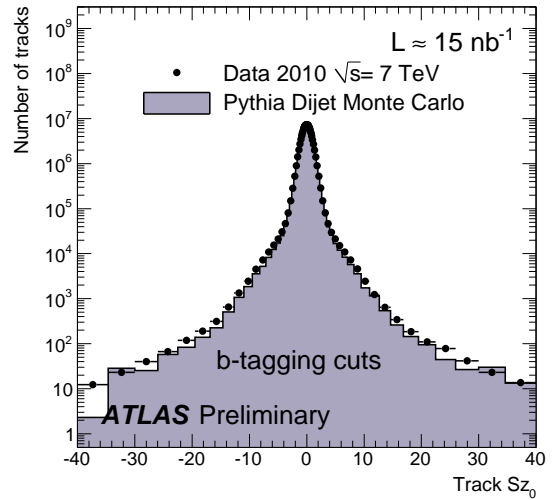
7
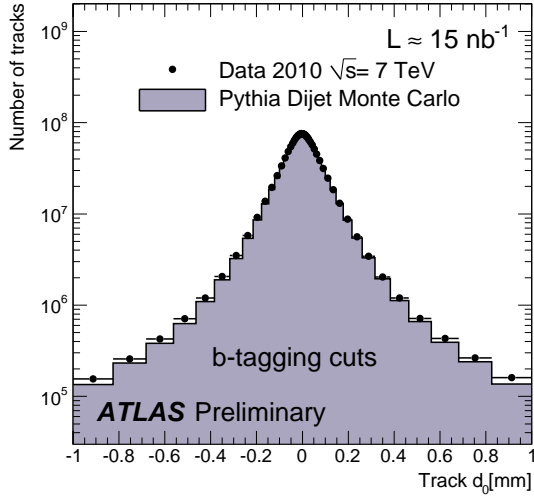
(a) Transverse impact parameter d_0.

(b) Impact parameter significance d_0/σ_{d_0}.

(c) Longitudinal impact parameter z_0.

(d) Impact parameter significance z_0/σ_{z_0}.

Figure 5: Distributions of impact parameters and their significance for tracks passing the b-tagging quality cuts. The upper plots are for the transverse impact parameter, the lower ones for the longitudinal impact parameter. Experimental data points are the solid black dots and the Monte Carlo simulation the plain histogram. The Monte Carlo is normalized to the data.

For this study, slightly different selection criteria are used than detailed earlier: the cuts on the impact parameters $|d_0|$ and $|z_0 \sin \theta|$ have been removed; all other cuts remain the same. The selected tracks have been divided into 15 p_T bins between 1 and 30 GeV and 16 θ bins. Twelve of these bins are in the barrel region ($0.19 \, \pi < \theta < 0.81 \, \pi$ which corresponds to $|\eta| < 1.2$).

As explained in Sec. 4.4, the track impact parameters are expressed at the point of closest approach in the transverse plane to the reconstructed event vertex. To extract the resolution, the distribution of impact parameters has been fitted within 2σ of its mean with a Gaussian function for each bin in θ and p_T. The width of this Gaussian $\sigma(d_0) = \sigma(d_0^{\mathrm{track}}) \oplus \sigma(PV)$ is understood as the impact parameter resolution convolved with the uncertainty of the reconstructed primary vertex.

5.1 Impact parameter resolution as a function of p_T and θ

Figure 6 shows a two-dimensional map of the d_0 resolution measured in experimental data, where the p_T of the tracks are shown along the x-axis and their θ along the y-axis. The value of the d_0 resolution follows the color coding on the right of the figure. As expected, Fig. 6 shows that the resolution of the transverse impact parameter d_0 has a strong correlation with both p_T and θ.

Figure 7 shows the ratio of the two-dimensional d_0 resolution between experimental and simulated data, where the p_T of the tracks are shown along the x-axis and their θ along the y-axis. The value of the d_0 ratio follows the color coding on the right of the figure. The agreement for small values of p_T is very good, for intermediate values around 6% and for large values ($p_T > 10$ GeV) the discrepancies are up to 15%.
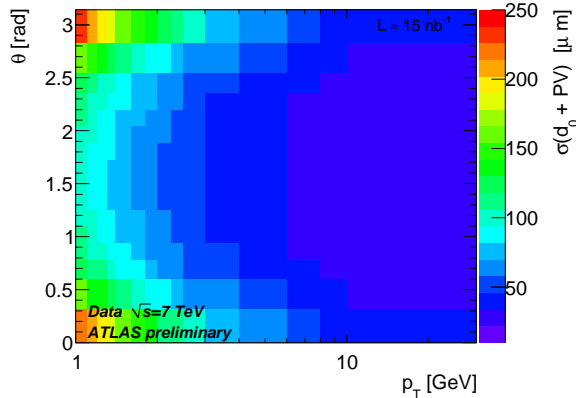

Figure 6: Two-dimensional map of the d_0 resolution measured in experimental data, where the p_T of the tracks are shown along the x-axis and their θ along the y-axis. $\theta = \frac{\pi}{2}$ refers to the centre of the detector.
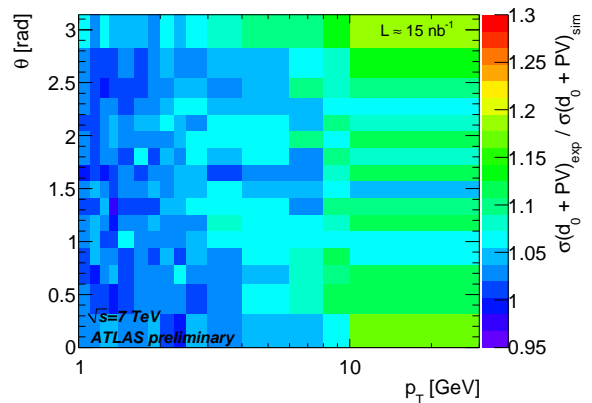
Figure 7: Two-dimensional ratio of the d_0 resolution between experimental and simulated data, where the p_T of the tracks are shown along the x-axis and their θ along the y-axis. $\theta = \frac{\pi}{2}$ refers to the centre of the detector.

To study the dependence of the transverse impact parameter resolution on p_T and θ in more detail, projections of the two-dimensional distributions of the resolutions onto single θ or p_T bins have been analysed. Figure 8 shows the d_0 resolution versus p_T for one central θ bin ($0.5 \, \pi < \theta < 0.55 \, \pi$). As expected, the resolution improves with increasing p_T. For this analysis the statistics are high enough to populate p_T bins up to 30 GeV. For fixed θ, the impact parameter resolution can be parameterized by the

EGN-Model [13]:

$$\sigma(d_0)_{\text{fixed }\theta} = \sqrt{E^2 + \frac{G^2}{p_T} + \frac{N^2}{p_T^2}} \, . \tag{1}$$

This model adds a linear term in $1/p_T$ compared to the simpler $A \oplus B$ model used in [5], where only two components, a constant term representing the intrinsic track resolution and a term in $1/p_T^2$ modeling the multiple scattering contribution, are present. While the latter model is not compatible with the experimental data up to high transverse momenta, the extended model describes all the experimental data starting from p_T values of 1 GeV very well, as shown in Fig. 8. The interpretation of the fit parameters, however, is not straightforward anymore. For example, this model allows no direct evaluation of the multiple scattering contribution to the impact parameter resolution. At the same time, the fit is useful to reduce the statistical uncertainty connected with the extraction of the resolution for a fixed p_T, shown in Table 1.
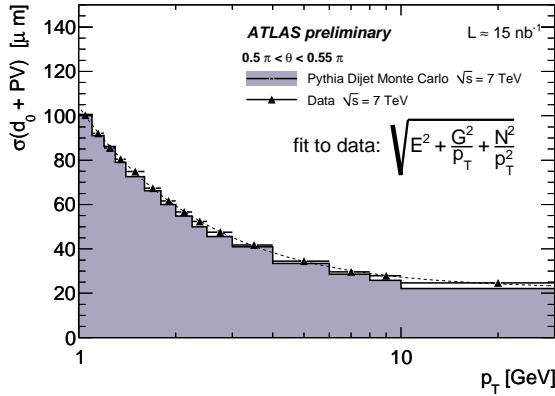

Figure 8: Transverse impact parameter resolution versus p_T for $0.5\,\pi < \theta < 0.55\,\pi$. The data have been fitted by $\sqrt{E^2 + \frac{G^2}{p_T} + \frac{N^2}{p_T^2}}$ (dashed line).
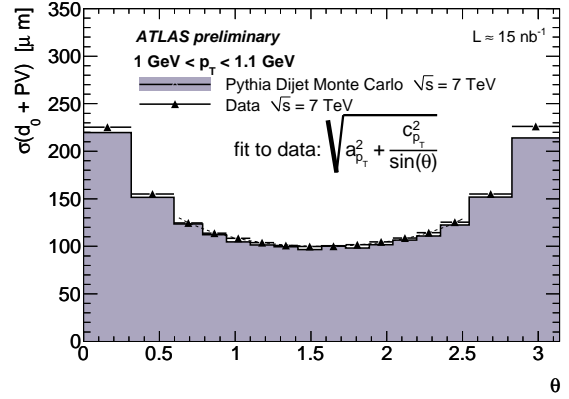
Figure 9: Transverse impact parameter resolution versus θ for 1 GeV$< p_T < 1.1$ GeV. $\theta = \frac{\pi}{2}$ refers to the centre of the detector. The data have been fitted by $\sqrt{a_{p_T}^2 + \frac{c_{p_T}^2}{\sin\theta}}$ in the barrel (dashed line).

Figure 9 shows the impact parameter resolution versus θ for one p_T bin (1 GeV$< p_T < 1.1$ GeV). $\theta = \frac{\pi}{2}$ refers to the centre of the detector. The dependence of the d_0 resolution on the traversed detector material and length of the extrapolation path between the silicon layers (i.e. θ) is clearly visible. Using Eq. 1, the parameterization for the transverse impact parameter resolution can be expressed as

$$\sigma(d_0)_{\text{fixed }p_T} = \sqrt{a_{p_T}^2 + \frac{c_{p_T}^2}{\sin\theta}} \quad \text{with} \quad a_{p_T} = \sqrt{E^2 + \frac{G^2}{p_T}} \quad \text{and} \quad c_{p_T} = \frac{b}{p_T} \, . \tag{2}$$

Both experimental and simulated data have been fitted by the formula in Eq. 2 (within $0.19\,\pi < \theta < 0.81\,\pi$).

Remaining small differences between experimental and simulated data can be potentially the result of the combined effect of residual misalignment in the detector and of differences in the primary vertex resolution, where the two effects cannot be easily disentangled. This will be studied in the next section.

5.2 Deconvolution of primary vertex errors

As already described, the impact parameter is expressed with respect to the primary vertex. This has the disadvantage of adding the primary vertex resolution to the intrinsic resolution of the track. Moreover,

even the *unbiased* primary vertex resolution depends on the p_T and θ of the single track, due to possible correlations of this track with the remaining tracks present in the same event: this potentially distorts the distribution of impact parameter resolution as a function of p_T and θ. The main aim of this section is to deconvolve the effect of the primary vertex resolution from the measurement of the impact parameter resolution itself.

5.2.1 Deconvolution method

The method relies on an *iterative* deconvolution procedure. The core of the impact parameter resolution can be described by the function:

$$R_{\text{meas}}(d_0) = \int \exp\left[-\frac{1}{2}\frac{d_0^2}{\sigma_{d_0,\text{trk}}^2 + \sigma_{d_0,\text{PV}}^2}\right] P\left(\sigma_{d_0,\text{PV}}\right) \mathrm{d}\sigma_{d_0,\text{PV}} \tag{3}$$

where the integrand is a Gaussian with a width corresponding to the square root of the squared average of the intrinsic track resolution $\sigma_{d_0,\text{trk}}$ and of the resolution of the primary vertex projected along the impact parameter direction $\sigma_{d_0,\text{PV}}$. This distribution is integrated over the distribution of values of resolutions of the primary vertex $P\left(\sigma_{d_0,\text{PV}}\right)$ corresponding to all the tracks considered. Since the primary vertex fit uses the beam-spot constraint, the beam-spot width is already included in the estimated uncertainty of the primary vertex. Starting from the distribution of Eq. 3, it is possible to obtain the deconvolved distribution by multiplying the measured impact parameter of each track by a correction factor

$$d_0 \to d_0 \cdot \left[1 + \frac{\sigma_{d_0,\text{PV}}^2}{\sigma_{d_0,\text{trk}}^2}\right]^{-1/2}. \tag{4}$$

Substituting this to Eq. 3, one moves from the distribution of R_{meas} to the distribution of R_{trk}

$$R_{\text{trk}}(d_0) = \exp\left[-\frac{1}{2}\frac{d_0^2}{\sigma_{d_0,\text{trk}}^2}\right]. \tag{5}$$

Since the correction factor depends on the track resolution $\sigma_{d_0,\text{trk}}^2$ to be measured, the procedure has to be applied iteratively. In addition, the study is performed in various ranges of track p_T and θ in order to ensure a quasi constant resolution within a single subset.

During the first iteration, individual values of the impact parameters of each track are modified according to Eq. 4, taking the initial ratio $\frac{\sigma_{d_0,\text{PV}}^2}{\sigma_{d_0,\text{trk}}}$ from the expected resolution $\sigma_{d_0,\text{PV,fit}}$ and $\sigma_{d_0,\text{trk,fit}}$, of the primary vertex and of the track fit. During this first iteration, the primary vertex error is not rescaled by a scale factor accounting for the different vertex resolution as provided by the primary vertex fit and the real vertex resolution in data since, in first approximation, the same scaling factor would affect the resolution of single tracks.

A new distribution is obtained by correcting all values of the impact parameter. This is then iteratively fitted with a Gaussian function in a $[-2\sigma, +2\sigma]$ range until the fitted σ is stable within 0.5%. The resulting value of σ represents the new estimate on the resolution $\sigma_{d_0,\text{trk}}$.

Next (i-th) iteration is then performed, where a different correction factor is applied:

$$d_{0,i} \equiv d_0 \cdot \left[1 + \frac{K_{\text{PV}}^2}{K_{\text{track},i-1}^2}\frac{\sigma_{d_0,\text{PV,fit}}^2}{\sigma_{d_0,\text{trk,fit}}^2}\right]^{-1/2}, \tag{6}$$

where d_0 is the value of the original impact parameter before the first iteration and the errors $\sigma_{d_0,\text{PV,fit}}$ and $\sigma_{d_0,\text{trk,fit}}$ are taken, track-by-track, from the nominal track and vertex fits, but where in addition the

11

scale factors K_{PV} for the primary vertex and $K_{\mathrm{track,i-1}}$ for the single track are introduced. The scale factor K_{PV} takes into account the difference in the resolution of the primary vertex in data with respect to the resolution predicted by the vertex fit: this accounts only for the intrinsic primary vertex resolution and not for the effect of the beam spot constraint. K_{PV} is obtained from an independent data-driven method, based on an analysis in which tracks forming the primary vertex are randomly split into two sets, two new primary vertices are fitted and their reconstructed positions are compared. The width of the *pulls*, defined as the separation between the two vertices $x_1 - x_2$ $(y_1 - y_2)$ divided by the error $\sqrt{\sigma_{x,1}^2 + \sigma_{x,2}^2}$ $\left(\sqrt{\sigma_{y,1}^2 + \sigma_{y,2}^2}\right)$, provides an estimate of the K factors, as presented in Ref. [14]. In order to cover possible model uncertainties, in this note, the width of the *pull* distribution is estimated in two complementary ways: first a fit with a Gaussian function is applied iteratively to the inner $[-2\sigma, +2\sigma]$ of the distribution, in the same way as done in Ref. [14], and then, as a second step, the Gaussian function fit is applied to the entire distribution. The K factor value is then taken as the average between the two and the uncertainty is inflated in order to cover the difference between the two measurements. The factor K_{PV} in events with $N_{\mathrm{tracks}} > 5$ in simulation is found to be 0.94 ± 0.02, while the same factor K_{PV} in data is found to be 0.97 ± 0.02. Given that the final primary vertex resolution combines the information from the bare vertex resolution with the constraint provided by the transverse beam spot width, which can be considered as well-calibrated within a systematic uncertainty of 2 %, the final K_{PV} is in between the value used and 1. Since at the present stage of the analysis the beam spot information is not avaible on an event-by-event basis, we cover possible differences in the relative contribution of the bare vertex resolution and the beam spot constraint by using $K_{\mathrm{PV}} = 0.97 \pm 0.05$ for simulation and $K_{\mathrm{PV}} = 0.985 \pm 0.05$ for data.

The scale factor K_{track} changes from iteration to iteration and is common for all tracks in a given p_{T} and θ range. and accounts for a similar resolution effect as in the vertex resolution description. $K_{\mathrm{track,i-1}}$ is the ratio of the estimated resolution $\sigma_{d_0, \mathrm{trk}}$ derived at the previous iteration $(i-1)$ of the method with respect to the resolution $\hat{\sigma}_{d_0, \mathrm{fit}}$ predicted by the fit errors of tracks in this p_{T} and θ range[2].

The procedure is repeated over and over and the correction of Eq. 6 applied until the measured resolutions $\sigma_{d_0, \mathrm{trk}}$ reach stability, for which typically three iterations are sufficient, even for the highest p_{T} bin (10–30 GeV).

5.2.2 Validation of the method

The method has been validated using Monte Carlo simulations by comparing the unfolded resolution to the true track resolution. The upper row of Fig. 10 shows the d_0 resolution as a function of track p_{T} (left) and the ratio to the true resolution (right) for a single θ interval. At high p_{T} the effect is larger because the primary vertex resolution contributes by a large fraction to the overall error, while the multiple scattering dominates the low p_{T} region. The unfolded resolution agrees with the true resolution within the quoted errors across the p_{T} range of $[0.5, 20]$ GeV. The errors include both the statistical uncertainty of the Gaussian fit and the systematic error caused by the limited precision with which the primary vertex error K_{PV} is known.

The same level of agreement can be observed for the transverse impact parameter resolution computed as a function of θ, as shown in bottom left plot in Fig. 10 together with the ratio to the true resolution (right), for a single p_{T} interval. The other p_{T} and θ intervals which are not shown in this note show the same level of agreement.

---

[2]To obtain the value of $\hat{\sigma}_{d_0, \mathrm{fit}}$ the impact parameter distribution is first obtained by randomly generating values of d_0 distributed according to a Gaussian function with a width corresponding to the distribution of $\sigma_{d_0, \mathrm{fit}}$ of all tracks in this bin. Then the predicted resolution value $\hat{\sigma}_{d_0, \mathrm{fit}}$ is obtained by using an iterative Gaussian fit in a $[-2\sigma, +2\sigma]$ range.
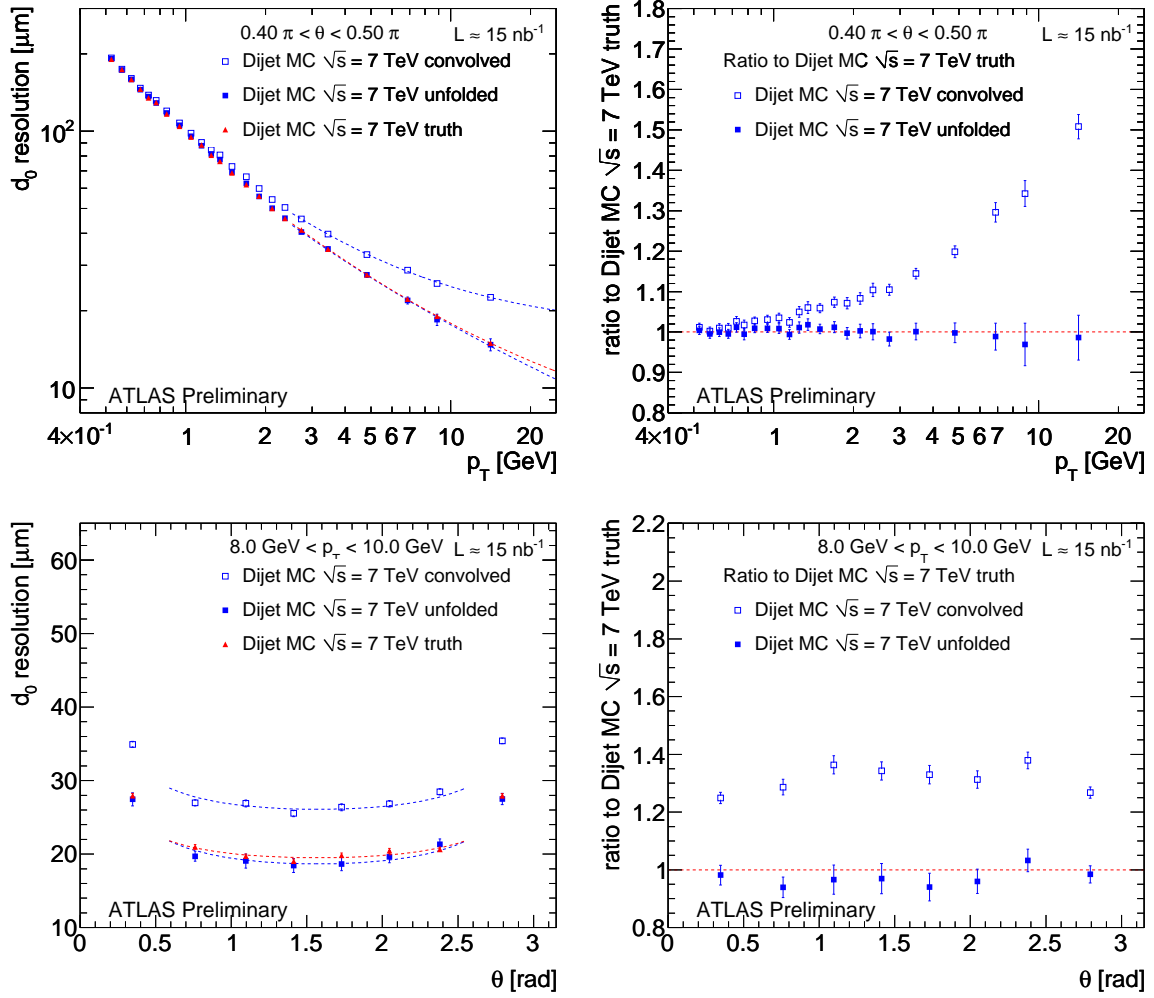
Figure 10: Top: transverse impact parameter resolution as a function of track p_T before and after unfolding as obtained by applying the deconvolution procedure on a Monte Carlo di-jet sample for tracks with $0.25\pi < \theta < 0.30\pi$, compared to the true resolution. Bottom: transverse impact parameter resolution as a function of track θ before and after unfolding as obtained by applying the deconvolution procedure to simulation for tracks with $(8 < p_T < 10)$ GeV, compared to the true resolution. Dashed lines on the left are fits to points.

5.2.3 Unfolded track impact parameter resolution in data

Next, the deconvolution procedure has been applied to data, in order to derive the unfolded track transverse parameter resolution as a function of p_T and θ and to compare it to the expectations provided by Monte Carlo simulations. This is shown in Fig. 11 as a function of p_T (top) for track directions θ in the interval of $0.40\pi < \theta < 0.50\pi$, as well as a function of θ (bottom) for tracks in the range $(8 < p_T < 10)$ GeV.
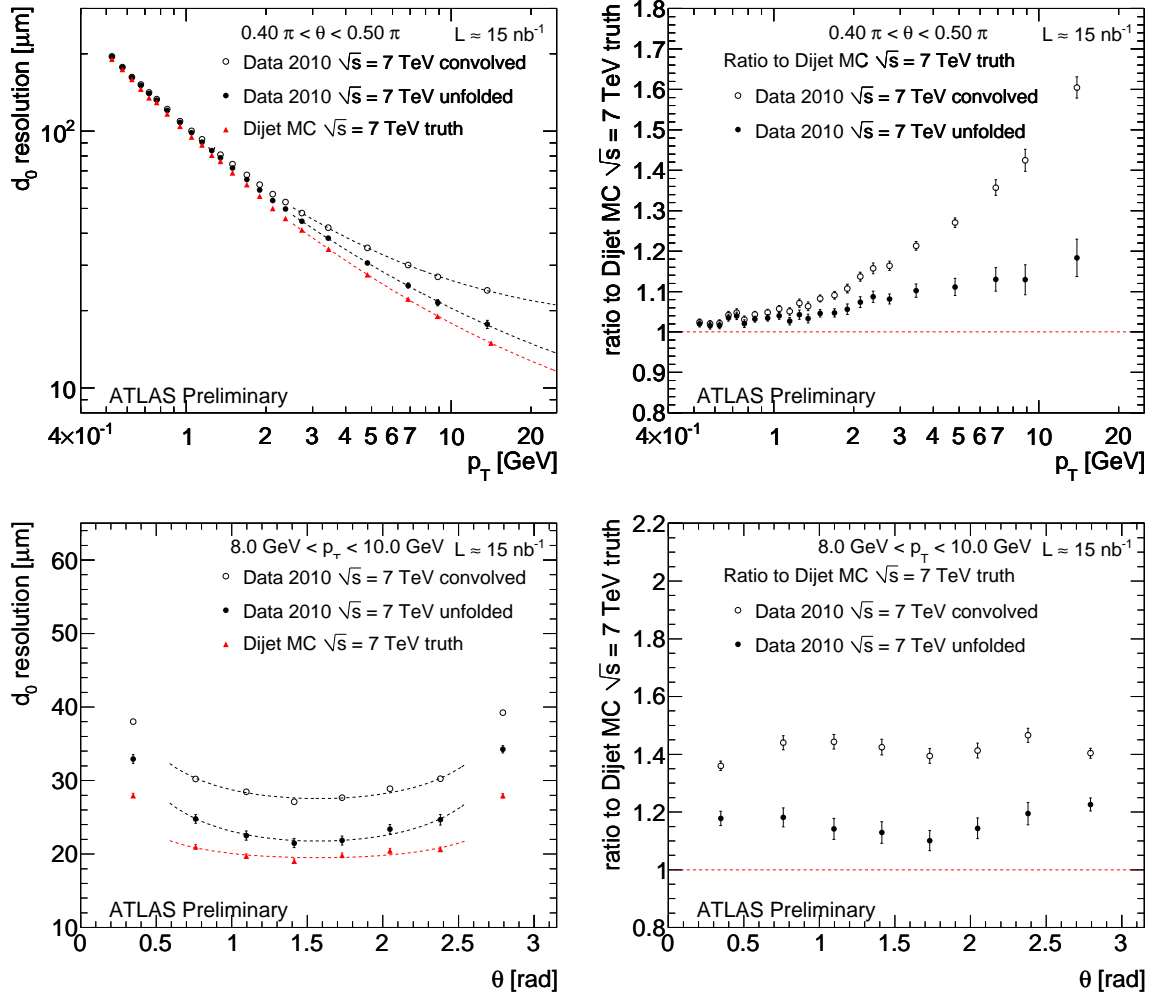

Figure 11: Top: unfolded transverse impact parameter resolution measured in data (full circles) as a function of p_T for values of $0.40\pi < \theta < 0.50\pi$, compared to the expectation from Monte Carlo simulations (triangles). For reference, also the resolution before unfolding is shown (open circles). Absolute values are shown on the left, while the ratios to the expected true resolution are shown on the right. Bottom: unfolded transverse impact parameter resolution measured in data as a function of θ for values of $(8 < p_T < 10)$ GeV, compared to the expectation from Monte Carlo simulations. For reference, also the resolution before unfolding is shown. Absolute values are shown on the left, while the ratios to the expected true resolution are shown on the right.

At low transverse momenta, where the multiple scattering and ionization loss are dominant, the simulation describes the impact parameter resolution correctly within few %, while a significant deviation is seen at values of p_T starting from a few GeV, reaching up to 20% at $p_T \approx 20$ GeV. This varies depending on the θ interval considered, as will be shown later. This possibly points to the presence of

residual misalignments in the detector.

While the extracted values of the resolution do not yet allow a precise estimate of the asymptotic resolution at very large p_T, it is however useful to compare precisely the resolution observed in data at $p_T = 15$ GeV with simulation, since around this p_T value the contribution of the multiple scattering term is expected to be comparable with the intrinsic resolution, so that this comparison is the most sensitive to differences in the intrinsic resolution between data and simulation.

In order to obtain a more precise estimate of this value, the transverse impact parameter resolution values for p_T in the range 2.5–20 GeV were interpolated with the function from Eq. 1. These fits versus p_T are already shown in Figs. 8, 10 and 11 (top left). They allow us to extract with increased statistical accuracy the resolution values in some θ bins for finite p_T values from the 7 TeV data . Table 1 shows these values for the convolved and the deconvolved transverse impact parameter resolution for values of p_T of 1 GeV, 5 GeV and 15 GeV in one central θ bin in the barrel and the end-cap (0.4 $\pi < \theta < 0.5 \pi$ and 0.9 $\pi < \theta < \pi$, respectively). Since the θ intervals chosen for this study are quite large, there is some residual dependence on the difference in the rapidity distribution of tracks between data and simulation: this adds a systematic uncertainty to the quoted numbers which is roughly estimated to be within 1%. The simulation uses a realistic detector description including the inefficiencies due to defect modules which were disabled during data taking.

| | | $\sigma(d_0)$ [μm] | | |
| | | *experimental data* | | *simulated data* |
	p_T	convolved	unfolded	MC truth
0.4 $\pi < \theta < 0.5 \pi$	1 GeV	104.0 ± 0.2	102.5 ± 0.3	98.2 ± 0.1
	5 GeV	34.2 ± 0.1	29.5 ± 0.2	27.2 ± 0.0
	15 GeV	23.9 ± 0.2	17.8 ± 0.5	15.4 ± 0.0
0.9 $\pi < \theta < \pi$	1 GeV	188.7 ± 0.2	188.2 ± 0.2	179.6 ± 0.0
	5 GeV	52.2 ± 0.1	48.3 ± 0.2	41.8 ± 0.0
	15 GeV	33.6 ± 0.1	28.0 ± 0.4	20.7 ± 0.0

Table 1: Resolutions of the transverse impact parameter for various values of transverse momentum for 7 TeV experimental and simulated data. The errors reflect the statistical uncertainties only, except for the unfolded resolutions, which also include the effect of systematic variations of the scale factor K_{PV}.

The transverse impact parameter resolution for tracks with momenta around $p_T = 15$ GeV are also shown in Fig. 12 as a function of θ. While in general the resolution predicted in the simulation is not far from the one assessed in data, some discrepancies are apparent, in particular in the two end-caps, the highest being in the forward region $\theta > 2.8$. Even if the accuracy of the alignment has been significantly improved before the last data re-processing, most of this discrepancy might still be explained by residual misalignment of the inner tracking detector, while an ideally aligned detector is assumed in the simulation.

Figure 13 shows that the impact of the primary vertex error on the convolved resolution is slightly stronger in simulation than in data. The main reason for this is that the beam spot width in simulation is significantly larger than in data (≈ 80 μm in simulation, while it can be as low as 30 μm in data). The deconvolution procedure is however taking this properly into account and the unfolded distributions are therefore not sensitive to this difference. In addition, the same figure also shows that the correction due to the unfolding procedure is not flat both in p_T and θ.

Figure 14 shows the two dimensional map of the deconvolved transverse impact parameter resolution. Figure 15 shows the ratio between the deconvolved d_0 resolution between experimental and simulated data.
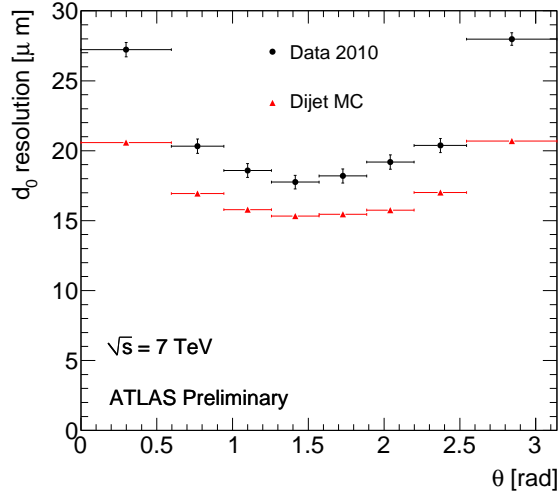
Figure 12: Unfolded impact parameter resolutions determined at $p_T = 15$ GeV as a function of θ, compared to the expected resolutions from Monte Carlo simulations, assuming a perfectly aligned detector.
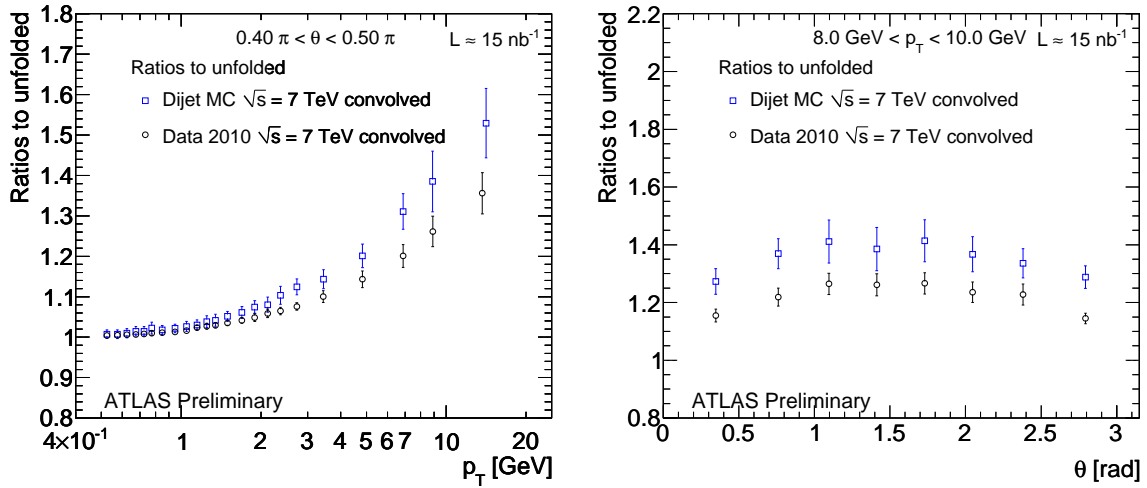

Figure 13: Ratio of the convolved impact parameter resolution to the unfolded one, both for Monte Carlo simulation and data, as a function of p_T for $0.25\pi < \theta < 0.30\pi$ (left) and as a function of θ for $(8 < p_T < 10)$ GeV.

6 Tracks in jets

The jet direction, calculated from the energy deposits in the calorimeters, is used to define a cone inside which tracks are associated to the jet, and also to define the sign of the impact parameter: the sign is positive if the track crosses the jet axis in front of the primary vertex and negative otherwise.

Complex track pattern-recognition issues may arise in a jet environment due to the high density of tracks. This may be particulary acute for narrow high-p_T jets.
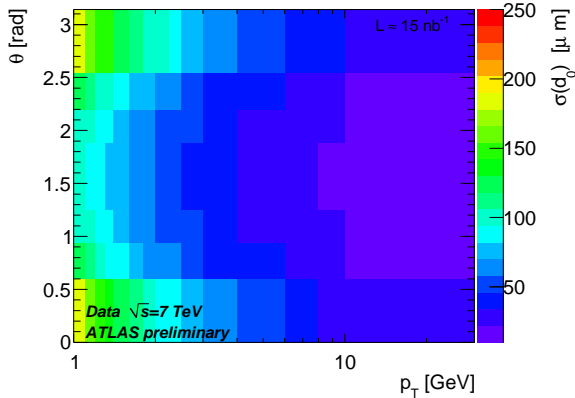
Figure 14: Two-dimensional map of the deconvolved d_0 resolution measured in experimental data, where the p_T of the tracks are shown along the x-axis and their θ along the y-axis. $\theta = \frac{\pi}{2}$ refers to the centre of the detector.
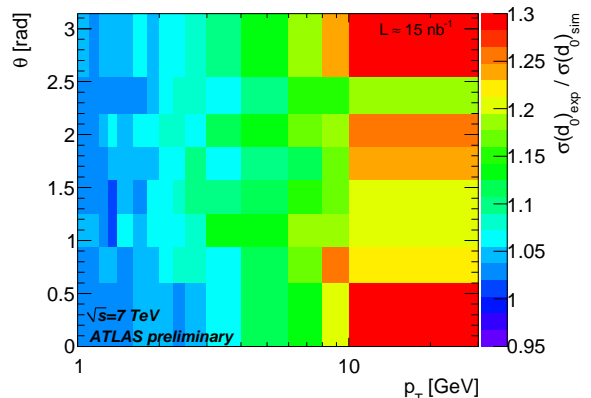
Figure 15: Two-dimensional ratio of the deconvolved d_0 resolution between experimental and simulated data, where the p_T of the tracks are shown along the x-axis and their θ along the y-axis. $\theta = \frac{\pi}{2}$ refers to the centre of the detector.

6.1 Tracks with shared hits

One important case for b-tagging is the case of tracks which are sharing some of their measurement points with other track(s). Shared hits occur more often in the silicon micro-strip detectors because these provide a precision measurement only in the $R\phi$ direction and only a loose constraint in the direction orthogonal to $R\phi$ (z in the barrel and R in the endcaps), despite the fact that the measurement layers are placed at larger radii. Thanks to its two-dimensional segmentation and high granularity, the pixel detector is more immune to this effect. Nevertheless, hit sharing in the pixel detector is actually more critical for b-tagging purposes since the lowest radius measurements define the impact parameter of the track. In the following, a track with shared hits is defined as having at least one shared hit in the pixels or at least two shared hits in the strips.

The distribution of the fraction of tracks with shared hits fulfilling the b-tagging quality cuts is shown as a function of their distance ΔR ($\sqrt{\Delta\eta^2 + \Delta\phi^2}$) to the b-tagging track under consideration in Fig. 16. It is clearly noticeable that the closer the tracks, the more likely they share hits, as expected. This effect is also quite well modeled by the simulation.

Despite being rather few, these tracks play a significant role in degrading b-tagging performance because they induce large tails in the d_0 distribution. This is shown for experimental data in Fig. 17 where those tracks are compared to tracks without shared measurements. This effect is reproduced fairly well by the simulation, as can be seen in Fig. 18. In the future, tracks with shared hits could be either removed or treated in a special way for b-tagging.

6.2 Jet selection

As mentioned already, calorimeter jets are used to define the jet direction which defines the associated tracks and the track's impact parameter sign. We have selected a sample of jets (cf. Ref. [2]) and have checked that the data is well modeled by the Monte Carlo. At least one track fulfilling the b-tagging quality cuts and associated to the jet with a spatial matching ΔR(jet, track) was required. The association cut varies as a function of the jet p_T, in order to have a smaller cone for jets at high p_T which are more collimated, but is around 0.4.
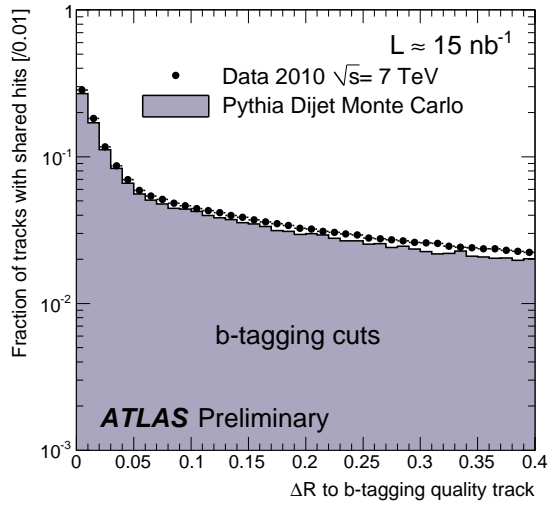
Figure 16: Distribution of the fraction of tracks with shared hits fulfilling the *b*-tagging quality cuts, as a function of their distance ΔR to the *b*-tagging quality track under consideration. Experimental data (solid black dots) are compared to the Monte Carlo simulation (plain histogram).
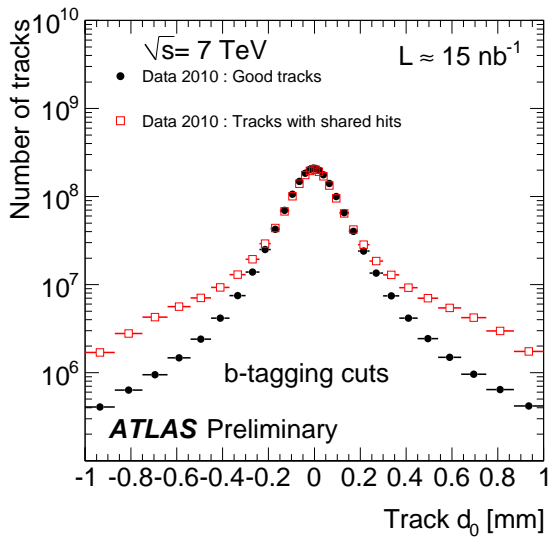

Figure 17: Distribution of the transverse impact parameter d_0 in experimental data for tracks without shared hits (solid black dots) and for tracks with shared hits (red open squares). The distribution for tracks with shared hits has been normalized to the same area of the distribution for tracks without shared hits.
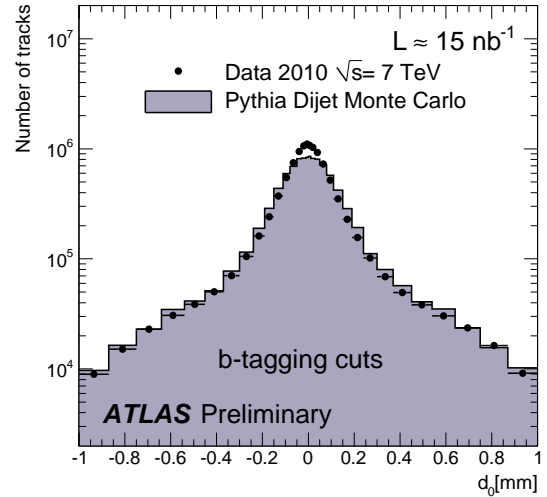

Figure 18: Distribution of the transverse impact parameter d_0 for tracks with shared hits in experimental data (solid black dots) and in simulated data (plain histogram). The Monte Carlo is normalized to the data.
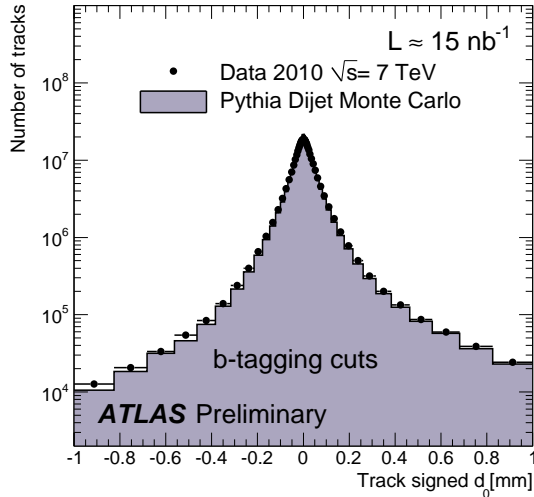
Figure 19: Distribution of the transverse impact parameter d_0 signed with respect to the jet axis. Experimental data (solid black dots) are compared to Monte Carlo simulation (plain histogram). The Monte Carlo is normalized to the data.
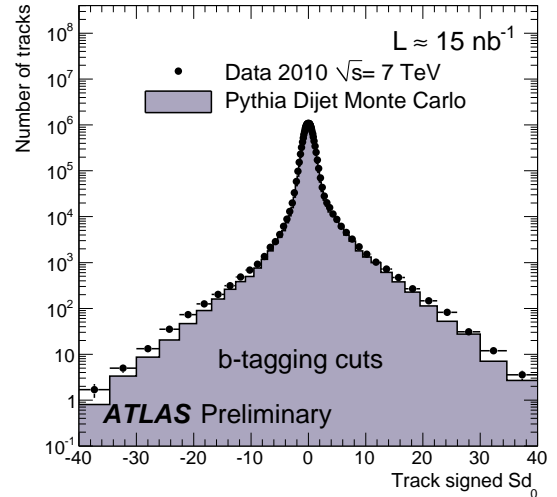
Figure 20: Distribution of the impact parameter significance d_0/σ_{d_0} signed with respect to the jet axis. Real data (solid black dots) are compared to Monte Carlo simulation (plain histogram). The Monte Carlo is normalized to the data.

6.3 Signed impact parameter

Figure 19 shows the distribution of the transverse impact parameter signed with respect to the jet axis, and Fig. 20 shows its significance. The impact parameter errors are not corrected according to results of the unfolding procedure presented in Sec. 5.2. The overall agreement between experimental data points and simulated data is good, though the simulated distributions are slightly narrower. The asymmetry induced by heavy flavour contributions (but also to a smaller extent K_s^0, Λ, photon conversions, etc) is clearly visible on both distributions.

The distributions in Fig. 18 and 19 show some discrepancies between experimental and simulated data. The overall impact parameter resolution (Fig. 19) is narrower in simulation compared to experimental data, as can be expected since *e.g.* the Inner Detector is perfectly aligned in simulation. The opposite effect can be observed for hits with shared tracks (Fig. 18), but it has to be noted that these tracks constitute only a very small fraction of all tracks. However, at the current early stage of the experiment the overall agreement is very satisfactory.

7 Conclusion

The analysis of the 7 TeV collision data taken by ATLAS shows that the Inner Detector and the track reconstruction are performing very well. The transverse impact parameter resolution of tracks was measured for the first time by unfolding the uncertainty connected with the reconstruction of the primary vertex. At low transverse momenta the resolution is well modelled in the simulation within few percent, confirming a good description of the multiple scattering and ionization losses due to material. At transverse momenta above $p_T = 1$ GeV some discrepancies start to get visible, pointing to the presence of residual misalignment of the inner tracking detector. These misalignments are known and are addressed by constantly improving the calibration and alignment of the inner tracking detector. The overall performance is very promising and these results point to the possibility of an early commissioning of ATLAS'

b-tagging capabilities.

References

[1] The ATLAS Collaboration, G. Aad et al., *Expected Performance of the ATLAS Experiment - Detector, Trigger and Physics*. No. CERN-OPEN-2008-020. 2009. `hep-ex:arXiv:0901.0512`.

[2] The ATLAS Collaboration, *Impact parameter-based b-tagging algorithms in the 7 TeV collision data with the ATLAS detector: the TrackCounting and JetProb algorithms*. No. ATLAS-CONF-2010-041. Geneva, June, 2010.

[3] The ATLAS Collaboration, *Performance of the ATLAS Secondary Vertex b-tagging Algorithm in 7 TeV Collision Data*. No. ATLAS-CONF-2010-042. Geneva, June, 2010.

[4] The ATLAS Collaboration, *Tracking studies for b-tagging with 900 GeV collision data with the ATLAS detector*. No. ATLAS-CONF-2010-003. Geneva, June, 2010.

[5] The ATLAS Collaboration, *Tracking studies for b-tagging with 7 TeV collision data with the ATLAS detector*. No. ATLAS-CONF-2010-040. Geneva, June, 2010.

[6] The ATLAS Collaboration, *Performance of the ATLAS jet trigger with pp collisions at sqrt(s)=900GeV*. No. ATLAS-CONF-2010-028. Geneva, May, 2010.

[7] The ATLAS Collaboration, *Properties of Jets and Inputs to Jet Reconstruction and Calibration with the ATLAS Detector Using Proton-Proton Collisions at $\sqrt{s}$ = 7 TeV*. No. ATLAS-CONF-2010-053. Geneva, July, 2010.

[8] T. Sjostrand, S. Mrenna, and P. Skands, *A Brief Introduction to PYTHIA 8.1.*, Tech. Rep. arXiv:0710.3820. CERN-LCGAPP-2007-04. LU TP 07-28. FERMILAB-PUB-07-512-CD-T, Oct, 2007.

[9] R. Frühwirth, W. Waltenberger, and P. Vanlaer, *Adaptive vertex fitting*, J. Phys. **G34** (2007) N343.

[10] The ATLAS Collaboration, *Charged particle multiplicities in pp interactions with a lowered pt threshold at sqrt(s) = 0.9 and 7 TeV measured with the ATLAS detector at the LHC*. No. ATLAS-CONF-2010-046. Geneva, Jun, 2010.

[11] The ATLAS Collaboration, *The ATLAS Experiment at the CERN Large Hadron Collider*, J. Instrum. **3** (2008) S08003.

[12] T. Cornelissen, M. Elsing, S. Fleischmann, W. Liebig, E. Moyse, and A. Salzburger, *Concepts, Design and Implementation of the ATLAS New Tracking (NEWT)*, Tech. Rep. ATL-SOFT-PUB-2007-007, CERN, Geneva, Mar, 2007.

[13] A. Salzburger, *A Parametrization for Fast Simulation of Muon Tracks in the ATLAS Inner Detector and Muon System. oai:cds.cern.ch:813003*. PhD thesis, Leopold-Franzens-Univ. Innsbruck, Innsbruck, 2003. Presented on 14 Jun 2003.

[14] The ATLAS Collaboration, *Performance of primary vertex reconstruction in proton-proton collisions at 7 TeV*. No. ATLAS-CONF-2010-069. Geneva, July, 2010.